Surface & Coatings Technology 444 (2022) 128663

Contents lists available at ScienceDirect

Surface & Coatings Technology

journal homepage: www.elsevier.com/locate/surfcoat

Surface hardness and corrosion behavior of laser surface-alloyed Ti6Al4V with copper

Q. Qiao [a], L.M. Tam [a,b], V.A.M. Cristino [a], C.T. Kwok [a,c,*]

[a] Department of Electromechanical Engineering, University of Macau, Macao
[b] Institute for Development and Quality, Macao
[c] Institute of Applied Physics and Materials Engineering, University of Macau, Macao

ARTICLE INFO

Keywords:
Laser surface alloying
Ti6Al4V
Copper
Hardness
Corrosion

ABSTRACT

Laser surface alloying of Ti6Al4V with different Cu contents (6, 8, 13 and 17 wt%) was successfully achieved using a high-power diode laser. With a higher Cu content, the grain size of the laser surface-alloyed Ti6Al4V specimens became finer, with more intermetallic phases (IMPs) formed and the hardness increased up to 646 ± 18 $HV_{0.2}$. Potentiodynamic polarization and electrochemical impedance spectroscopy (EIS) were conducted to study the corrosion behavior of the laser surface-alloyed specimens in a 0.9 wt% NaCl solution at 37 °C. It was found that the specimen alloyed with 6 wt% Cu showed the mild micro-galvanic effect between $CuTi_2$ and α-Ti. The specimen with 17 wt% Cu had the highest content of IMPs and possessed the lowest corrosion resistance due to the most significant micro-galvanic effect between the IMPs (cathode) and the α-T / β-Ti matrix (anodes). With an appropriate Cu content, laser surface-alloyed Ti6Al4V can also act as hard and corrosion resistant components possessing a high anti-bacterial efficacy by virtue of Cu.

1. Introduction

Recently, titanium (Ti) alloys have attracted a lot of attention for biomedical and engineering applications due to their low density, outstanding mechanical strength and excellent corrosion resistance and good biocompatibility [1–3]. Applications of pure Ti are limited due to its low yield strength [4,5]. Addition of alloying elements including Al, V, Cu, and Ag are well-documented and widely applied to enhance the properties of the alloys [6,7]. A previous study reported that the mechanical strength of cast Ti—Cu alloys for dental applications was higher than that of cast pure Ti [8]. However, it is also well-known that the high mechanical strength of the Ti-based alloys leads to difficulty in manufacturing and post-processing with conventional techniques [9–11]. Compared to pure Ti, Ti—Cu alloys fabricated by powder metallurgy possess better mechanical properties and stronger antibacterial activity [12]. It was reported that Ti—Cu alloys fabricated using spark plasma sintering showed higher hardness and yield strength [13]. On the other hand, inhibiting bacterial adhesion and growth on metallic public facilities and clinical devices, odontological and orthopedic metallic implants plays a crucial role in preventing infection and keeping biological safety. Even though Ti alloys cannot completely get rid of bacterial adhesion, it is possible to be controlled and mitigated via surface modification [3]. The aforesaid fabrication methods are challenged by existence of porosities, phase transformation, oxidation and grain growth [13]. Whereas, laser surface alloying (LSA) is an effective surface modification technique which offers unique merits over other methods, including high throughput speed, process compatibility, high processing efficiency and good surface uniformity [14,15]. Meanwhile, the rapid self-quenching in LSA results in a stronger metallurgical bond between the alloyed layer and substrate, the formation of a non-equilibrium or amorphous phase as well as homogenization and refinement of the microstructure, all without affecting the bulk properties of the substrates [16]. In addition, the existing or defective components made of Ti alloys can be remanufactured via LSA for conservation of energy and materials. Recently, LSA has been widely applied in medical, aerospace, automobile, nuclear, mining, and refinery industries [17–19].

There are some investigations on the microstructure and antibacterial properties of Ti6Al4V and Ti—Cu alloys [12,20–23]. It is reported that the Cu-bearing Ti alloys exhibit strong antibacterial property. The antibacterial mechanism was thought to be associated with the Cu ion released from the Cu-bearing Ti alloys. However, the effect of Cu on the corrosion performance of the Cu-bearing Ti-alloys is controversial. Takada and Okuno [24] investigated the corrosion behavior of arc-

* Corresponding author at: Department of Electromechanical Engineering, University of Macau, Macao.
E-mail address: fstctk@um.edu.mo (C.T. Kwok).

https://doi.org/10.1016/j.surfcoat.2022.128663
Received 8 May 2022; Received in revised form 24 June 2022; Accepted 24 June 2022
Available online 1 July 2022

melted Ti—Cu alloys with 5–20 wt% Cu. It was found that the passive region of the Ti—Cu alloys was extended by 1.4 V in 0.9 wt% NaCl solution at 37 °C. While the increase in current density in the transpassive region (above 1.4 V) was small and the anodic polarization curve did not appear to break down although the surface area of $CuTi_2$ was larger [24]. On the other hand Osorio et al. [25] reported that the corrosion current density of centrifuge-cast Ti—Cu alloys (5–15 wt% Cu) containing $CuTi_2$ increased with the increase in Cu content in 0.15 M NaCl solution at 25 °C. Qin and his co-workers [3] found that Ti-5wt%Cu formed by selective laser melting (SLM) showed an extremely non-uniform distribution of $CuTi_2$ in the α-Ti matrix but the polarization curves still had a board passive range (0.6–1.2 V) in Hanks' solution at 37 °C. Ren and co-workers [21] reported that addition of 1–5 wt% Cu in Ti6Al4V using vacuum arc melting did not affect the corrosion resistance in the 0.9 wt% NaCl solution at 37 °C and the alloys possessed pitting potentials higher than 1.2 V. SLMed Ti6Al4V alloys with 2–6 wt% Cu possessed higher corrosion resistance than that of Ti6Al4V alloy in the 0.9 wt% NaCl solution at 37 °C and the one with 4 wt% Cu displayed the most outstanding corrosion resistance [22]. On the other hand, it was reported that the existence of $CuTi_2$ in the Ti—Cu alloys showed a significant influence on mechanical properties [23]. The microhardness of Ti-10wt%Cu was three times higher than that of cp-Ti owing to the strong strengthening effect of the nano-scale Ti_2Cu particles. Nevertheless, the addition of anti-bacterial elements like Cu to the Ti alloys using LSA to assess the influence of microstructure on the mechanical and corrosion behavior has not been reported in the literature.

Fabrication of an anti-bacterial Cu-bearing coating on an existing Ti alloy via LSA is of practical interests; therefore, it is essential to investigate the relationship between the microstructure and surface properties (hardness and corrosion resistance). In this study, adding Cu to Ti6Al4V via LSA was attempted. The Cu content in Ti6Al4V was controlled using various laser processing conditions resulting in different microstructure, hardness and corrosion resistance. The acquired experimental results can provide useful guidelines for marine, clinical and medical applications of Ti6Al4V laser surface-alloyed with Cu.

2. Experimental details

2.1. Materials and specimen preparation

The Ti6Al4V plates of dimensions of 25 mm × 25 mm × 3.9 mm were used as the substrate in LSA, and the chemical compositions of the alloy are shown in Table 1. The plates were ground with the 80-grit SiC paper to remove surface impurities and increase the roughness for adhesion with the Cu powder. Then the plates were ultrasonically cleaned in ethanol followed by washing in distilled water. The Cu powder (purity: 99.9 %) with average particle size of 75 μm was mixed with 4 wt% polyvinyl alcohol to become a slurry, and preplaced on the surface of the Ti6Al4V plates using a paintbrush. The thickness of the preplaced Cu layer was controlled to be 0.025 mm and 0.05 mm. All the preplaced specimens were dried with a heating fan before LSA.

Table 1
Chemical compositions of pristine Ti6Al4V and laser surface-alloyed specimens.

Specimens*	Al (wt%)	V (wt%)	Cu (wt%)	Ti (wt%)
Ti6Al4V	6.10 ± 0.10	3.60 ± 0.30	0.00 ± 0.00	Bal.
LA-Ti64-6Cu	5.89 ± 0.05	2.84 ± 0.44	6.00 ± 0.12	Bal.
LA-Ti64-8Cu	5.94 ± 0.06	3.42 ± 0.13	8.07 ± 0.46	Bal.
LA-Ti64-13Cu	5.20 ± 0.10	2.92 ± 0.22	13.07 ± 0.81	Bal.
LA-Ti64-17Cu	5.35 ± 0.13	3.24 ± 0.05	17.14 ± 0.69	Bal.

* *x* in the designation 'LA-Ti64-*x*Cu' represents the maximum Cu content (in wt%).

2.2. Laser surface alloying (LSA)

LSA of Ti6Al4V preplaced with Cu powder was implemented using a 2.3 kW continuous wave (CW) high-power diode laser (HPDL) module (Laserline, LDM 1000–1000) with a beam diameter of 2 mm at a power of 2 kW and scanning speeds of 20, 30 and 40 mm/s (Fig. 1). The wavelength of the HPDL (990 nm) could offer the laser absorptivity by Ti and Cu at 65 % and 9 % respectively [26]. The laser surface-alloyed specimens with various Cu contents were obtained by adjusting the average thickness of the preplaced Cu layer (0.025 and 0.05 mm) and the scanning speed of the laser beam (20, 30 and 40 mm/s) during the laser surface alloying process. After precise weighing of the specimens before and after preplaced with the Cu layer using an electronic balance (with an accuracy of ±0.1 mg), the average thickness (T) of preplaced layers was calculated using eq. (1):

$$T = \text{mass of the Cu layer}/(\text{area of surface} \times \text{density of Cu}) \quad (1)$$

A thicker preplaced Cu layer allows a higher Cu content to be alloyed in the alloyed zone. On the other hand, a higher laser scanning speed allows a shorter interaction time between the laser beam and the preplaced specimen leading to a lower degree of dilution and hence a higher Cu content. From Fig. 1, the LSA process was carried out with a gas shroud cover, and the oxidation of the specimen was mitigated by introducing Argon gas flowing at a rate of 15 L/min for shrouding the processing region. The arrows show the raster pattern of laser beam and overlapping of successive parallel laser-alloyed tracks with an overlapping ratio of 50 %. As there is space between particles in the preplaced Cu layer, the approximate dilution ratio (DR) corresponding to the degree of dilution of Cu in the alloyed zone is defined as follows:

$$DR = \left(1 - \frac{T}{D}\right) \times 100\% \quad (2)$$

where T is the preplaced coating thickness of the Cu layer and D is thickness of the alloyed layer. According to the definition, a larger DR corresponds to a higher degree of dilution (lower Cu content). After LSA, the specimens were cross-sectioned for further metallographic and microstructural analyses. The specimens were ground with 400, 600, 800-grit SiC papers and then polished with 6 and then 1-μm diamond pastes successively. Lastly, the polished specimens were cleaned with ethanol to remove any remaining dirt and oil, and etched with acidified ferric chloride solution (mixture of 100 mL ethanol, 5 g $FeCl_3$ and 15 mL HCl) for studying the microstructure (Fig. 2).

2.3. Materials characterization

Phase analysis was conducted with an X-ray diffractometer (XRD), Rigaku MiniFlex 600, with Cu Kα radiation operated at 40 kV and 40 mA, and a scanning rate of 0.25°/s. The XRD patterns of the pristine Ti6Al4V and the laser surface-alloyed specimens were obtained. A scanning-electron microscope (SEM), Hitachi S-3400 N, equipped with a Horiba EX-250 energy dispersive X-ray spectrometer (EDS) was used to investigate the microstructure and compositions of the cross-sections of the alloyed specimens.

2.4. Hardness tests

The hardness along the depths of cross-section of the laser-alloyed specimens were measured using a micro-hardness tester (VH3100, Buehler, Germany) with a load of 200 g and a loading time of 10 s. At least 5 locations were chosen for hardness testing to ensure the repeatability of the experimental results and the average microhardness values were then calculated.

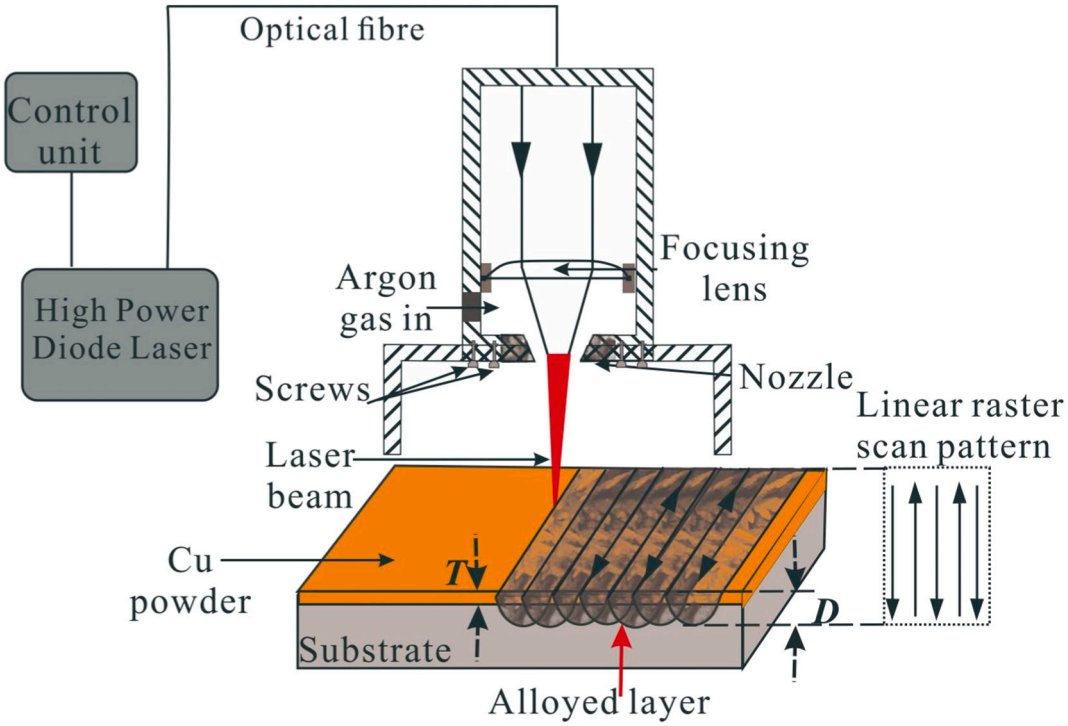

Fig. 1. Schematic representation of the LSA process.

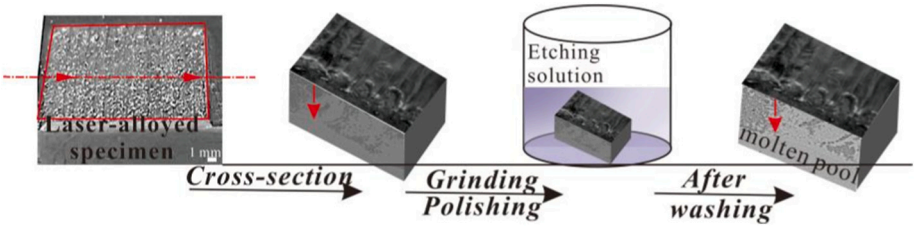

Fig. 2. Specimen preparation for metallographic and microstructural analyses.

2.5. Electrochemical measurements

Before the electrochemical tests, the specimens were ground with 800-grit SiC paper and mounted in the epoxy resin. As illustrated in Fig. 3, the corrosion tests were conducted in stagnant 0.9 wt% NaCl solution with a potentiostat (PAR VersastatII). The temperature of the solution was maintained at 37 ± 1 °C using an electronic water bath. The electrochemical tests were conducted in 0.9 wt% NaCl solution and 37 ± 1 °C to simulate the human body environment. The potential was measured with respect to standard calomel electrode (SCE, +0.244 V vs. SHE at 25 °C) as the reference electrode. Two parallel graphite rods served as the counter electrodes for current measurement. The specimens served as the working electrode with an exposed area of about 1 cm^2. Prior to potentiodynamic polarization test [27], open-circuit potential (E_{OCP} vs. SCE) measurements were conducted for 2 h for the specimen to reach a steady-state condition. Then the potential was increased at a rate of 0.167 mV/s, begin with 0.2 V vs. SCE below the free corrosion potential. The corrosion potential (E_{corr} vs. SCE) and the corrosion current density (I_{corr}) were extracted using Tafel extrapolation with the software PowerCorr.

The calculation of the densities ρ (g/cm^3) of the laser-alloyed layers was based on the weight fractions of Ti, V, Al and Cu by the rule of mixture:

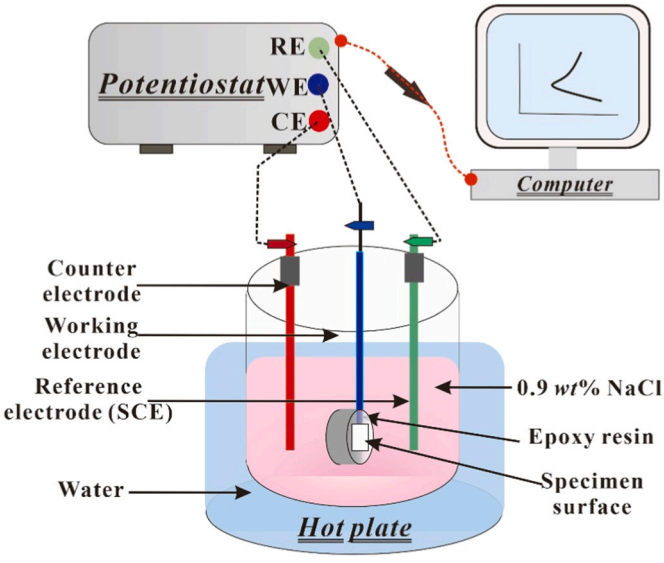

Fig. 3. Schematic representation of the corrosion tests conducted in 0.9 wt% NaCl solution at 37 ± 1 °C.

$$\rho = \left(\frac{W_{Ti}}{\rho_{Ti}} + \frac{W_V}{\rho_V} + \frac{W_{Al}}{\rho_{Al}} + \frac{W_{Cu}}{\rho_{Cu}}\right)^{-1} \quad (3)$$

where $\rho_{Ti} = 4.51$ g/cm^3, $\rho_V = 6.11$ g/cm^3, $\rho_{Al} = 2.70$ g/cm^3 and $\rho_{Cu} = 8.94$ g/cm^3 are the theoretical densities of Ti, Al, V and Cu respectively, and the weight fractions of Ti, Al, V and Cu in the laser-alloyed layer are W_{Ti}, W_{Al}, W_V and W_{Cu} respectively ($W_{Ti} + W_{Al} + W_V + W_{Cu} = 1$). The corrosion rate ($r$, mm/yr) of the specimen was calculated from I_{corr} according to ASTM Standard G102–89 [28]:

$$r = K\left(\frac{I_{corr}}{\rho}\right)EW \quad (4)$$

where K is a constant $= 3.27 \times 10^{-3}$ mm g μA^{-1} cm^{-1} yr^{-1}; I_{corr} is in μA/cm^2; ρ is the density obtained from eq. (3) in g/cm^3 and EW is the equivalent weight, which is defined as follows:

$$EW = \left(\sum \frac{n_i W_i}{A_i}\right)^{-1} \quad (5)$$

where W_i is the weight fraction; n_i is the valence; and A_i is the atomic mass of the i^{th} element in the specimen.

After the polarization tests, the specimens were ultrasonically cleaned in distilled water for 10 min and their corrosion morphologies were investigated using SEM. Electrochemical impedance spectroscopy (EIS) measurements were done at E_{OCP} vs. SCE over the frequency range from 100 kHz to 10 mHz with an amplitude of 10 mV. In order to analyze the EIS results, an appropriate model (ZView) has been used for equivalent circuit quantification. All electrochemical tests were performed at least three times to ensure the repeatability of the results.

3. Results and discussion

3.1. Microstructure

Fig. 4 shows the compositional profiles of various elements along the depth of Ti6Al4V laser surface-alloyed with Cu. Fig. 5(b) depicts the variation of the Cu content along the depth, the average thickness of the alloyed layer and the *DR* of the laser-alloyed specimens. Under the same laser power, a higher scanning speed led to a shorter interaction time between the laser beam and the specimens [29], and a smaller total volume or a thinner alloyed layer formed with a higher quenching rate. Hence, the thickness of the alloyed layer decreases and the Cu content in the alloyed layer increases. The average thicknesses of the laser surface-alloyed layers obtained from five different locations are in the range from 0.78 to 1.07 mm (Fig. 5(b) and Table 2). The maximum Cu contents of the alloyed layers is ranging from 6 to 17 wt% (Fig. 5(b) and Table 2). The laser surface-alloyed specimens are designated as LA-Ti64-*x*Cu where *x* represents the maximum Cu content (in wt%).

The microstructure of the laser surface-alloyed specimens depends on the laser processing parameters and the Cu content [30,31] (Fig. 6). No cracks and defects are observed in the alloyed zones and at the interfaces between the alloyed layers and the substrate of all the specimens [Fig. 6(a-I, b-I, c-I and d-I)] and all alloyed layers are metallurgically bonded to the substrate. After LSA, the high temperature and high cooling rate led to rapid heat conduction in the substrate, which in turn induced directional dendritic growth and refined microstructure in the alloyed layers (Fig. 6) [32,33]. In addition, the XRD patterns of the specimens and the pristine Ti6Al4V are presented in Fig. 7 for phase identification.

Cu is a β-stabilizing element for the Ti alloys. Collings and Gegel [34] indicated that Cu atoms aggregate easily in the Ti alloys, leading to enhanced local accumulation of Cu atoms in the Ti-matrix. Then the

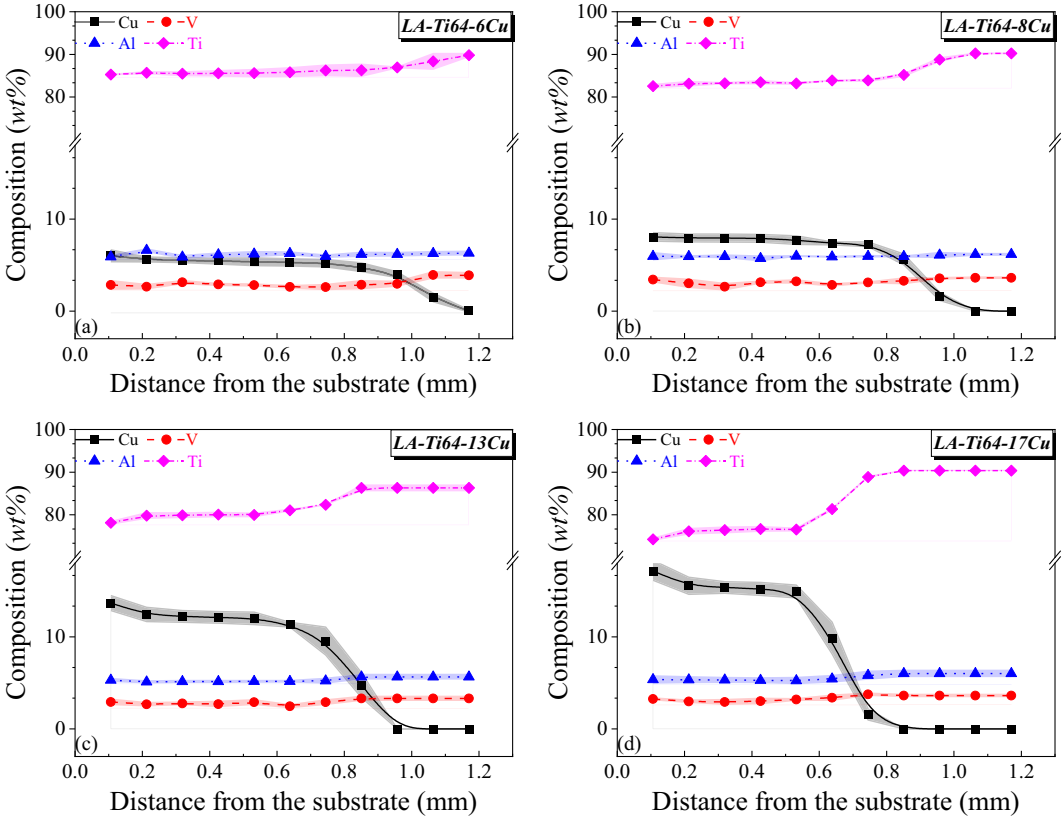

Fig. 4. Compositional profiles of laser surface-alloyed specimens fabricated at various preplaced thicknesses and scanning speeds: (a) LA-Ti64-6Cu, (b) LA-Ti64-8Cu, (c) LA-Ti64-13Cu and (d) LA-Ti64-17Cu.

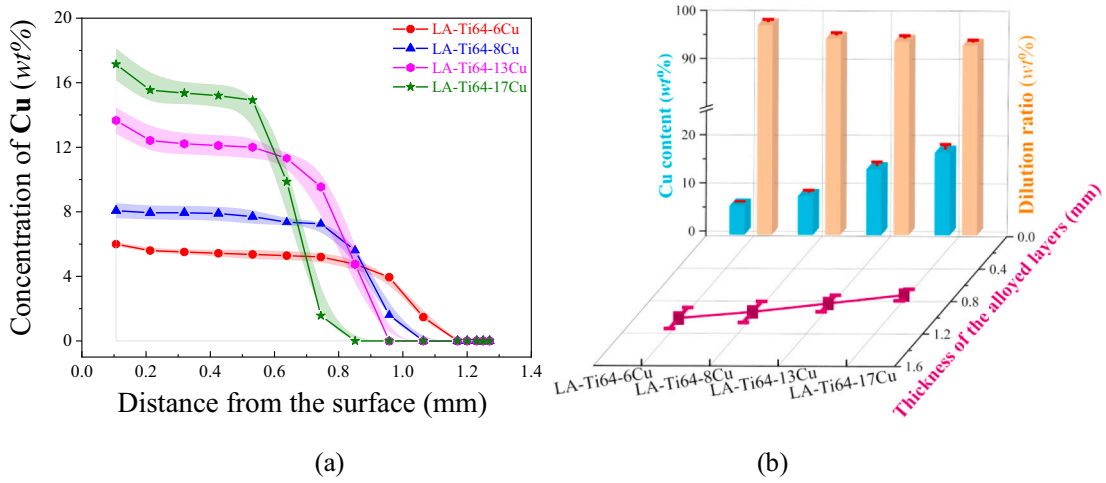

Fig. 5. (a) Cu content along the depth and (b) thickness of the laser surface-alloyed layer, dilution ratio and maximum Cu content of various laser-alloyed specimens.

Table 2
LSA parameters, maximum Cu content and dilution ratio for the laser-alloyed specimens.

Specimens	Thickness of preplaced Cu (*T* / mm)	Scanning speed (*v* / mm/s)	Thickness of alloyed layer (*D* / mm)	Maximum Cu content (*wt*%)	Dilution ratio (*DR* / %)
LA-Ti64-6Cu	0.025	20	1.07	6.00	97.7
LA-Ti64-8Cu	0.050	20	0.99	8.07	94.9
LA-Ti64-13Cu	0.050	30	0.89	13.07	94.4
LA-Ti64-17Cu	0.050	40	0.78	17.14	93.6

non-uniform nucleation sites would induce the formation of $CuTi_2$ precipitates. Since the lattice distortion near Cu-rich clusters provided energy to overcome nucleation barriers and facilitated $CuTi_2$ nucleation [35], a higher Cu content would cause more $CuTi_2$ precipitates. The equilibrium phase diagram of the Ti—Cu system [30] shows the formation of eutectoid alloy (α-Ti + $CuTi_2$) with 7 wt% Cu. A Cu content of 6 and 8–17 wt% in the laser surface-alloyed specimens corresponds to the hypo-eutectoid and the hyper-eutectoid compositions, respectively.

Fig. 6(a-II and III) depicts a dendritic structure in LA-Ti64-6Cu containing α-Ti as the major phase as confirmed by the XRD patterns (Fig. 7). Under a higher magnification, the Cu-rich IMPs (brighter zones) and α-Ti (darker zone) can be observed in LA-Ti64-6Cu [Fig. 6(a-III)]. According to the EDS line scanning from X to Y, a significant increase in Cu content, and decrease in Ti and Al contents are detected. It is due to transition from the metallic phase α-Ti to the IMPs. From the XRD patterns of LA-Ti64-6Cu (Fig. 7), most of the diffraction peaks correspond to α-Ti and some minor peaks to $CuTi_2$ and β-Ti are also detected. Due to the eutectoid reaction, β-Ti in the LA-Ti64-6Cu entered the eutectoid transformation region as the temperature decreased. Then, Cu was used to form $CuTi_2$ due to its supersaturation in the β matrix. There was also a local metastable balance between β-Ti and $CuTi_2$, forming a Cu-deficient region near the $CuTi_2$ nucleation sites, which facilitated α-Ti to nucleate [36]. Meanwhile, Cu was absorbed for the growth of $CuTi_2$, which was the minor phase present in the alloyed layer [37]. From the Ti—Cu phase diagram [30], the reaction for the LA-Ti64-6Cu with hypoeutectoid composition (6 wt%) is as follows:

$$L \rightarrow L + \beta - Ti \rightarrow \beta - Ti \rightarrow \alpha - Ti + \beta - Ti \rightarrow \alpha - Ti + CuTi_2 \quad (6)$$

Fig. 6(b)-(c) displays the microstructures of LA-Ti64-8Cu and LA-Ti64-13Cu with hypereutectoid compositions, which are mainly composed of $CuTi_2$ (brighter zone) embedded in *α*-Ti (darker zones) [38]. From Fig. 6(b-III) and (c-III), a dramatical drop in Ti content in the brighter zone is observed, accompanied with the increase in the Al and Cu contents. Compared to LA-Ti64-6Cu, more IMPs ($CuTi_2$ and CuTi) are detected in the XRD patterns of LA-Ti64-8Cu and LA-Ti64-13Cu (Fig. 7) due to rapid cooling and solidification. The amount of the IMPs increases with the increase in the Cu content, which is consistent with the finding of Xu and co-workers [39]. The IMPs were formed in LA-Ti64-8Cu and LA-Ti64-13Cu via the following reactions [40]:

$$L \rightarrow L + \beta - Ti + CuTi_2 \rightarrow \beta - Ti \rightarrow \beta - Ti + CuTi_2 \rightarrow \alpha - Ti + CuTi_2 \quad (7)$$

$$L \leftrightarrow CuTi_2 + CuTi \quad (8)$$

LA-Ti64-17Cu with the highest Cu content contains a dendritic structure as shown in Fig. 6(d-II). The grain size of LA-Ti64-17Cu processed under a higher scanning speed (40 mm/s) is smaller (about 2 μm) than those of LA-Ti64-8Cu (about 50 μm) and LA-Ti64-13Cu (about 37 μm). In fact, Cu was a potential grain refiner for Ti6Al4V [41]. Previous studies have reported that the equiaxed grains were formed when 6.8 wt % Cu was added to Ti6Al4V [36]. Addition of Cu reduced the lattice parameters and also led to the formation of finer grains. No new phase is found in LA-Ti64-17Cu but the volume fraction of the IMPs ($CuTi_2$ and CuTi) further increases as the dominant phases (Fig. 7). A higher laser scanning speed leads to a shorter interaction time between the laser beam and the materials (powder and substrate) and could lead to a higher cooling rate and a finer grain size after rapid solidification [42–44]. The pristine Ti6Al4V consists of uniformly distributed α-Ti and β-Ti [45] with a larger grain size (76 μm) [Fig. 6(e)]. The existence of α-Ti and β-Ti is also evidenced by their diffraction peaks in the XRD patterns (Fig. 7).

The compositional analyses at the selected locations of the LA-Ti64-6Cu and LA-Ti64-17Cu are shown in Fig. 8. For LA-Ti64-6Cu, the alternating dendritic structure of bright pro-eutectoid α-Ti and dark $CuTi_2$ can be observed in Fig. 8(a-I) and the EDS spectra are depicted in Fig. 8(b). Sites A and B in Fig. 8(a-I) demarcate the two distinct phases in the dendritic structure. The darker site (A) with 90.92 at.% Ti, 5.74 *at.*% Al, 2.08 at.% V and 1.26 at.% Cu, corresponds to α-Ti phase detected in the XRD patterns. Brighter site (B) contains 64.12 at.% Ti, 6.02 at.% Al, 1.41 at.% V and 28.45 at.% Cu, indicating that the atomic ratio of Ti and Cu is approximately 2:1, which corresponds to the IMP $CuTi_2$.

On the other hand, the clusters of darker phases (α-Ti, marked as 'C') in the matrix of brighter IMPs (marked as D, E, and F) are observed in LA-Ti64-17Cu [Fig. 8(a-II)]. The sizes of the α-Ti are finer than that of the LA-Ti64-6Cu. EDS spectra indicate that the dark phase (C), which

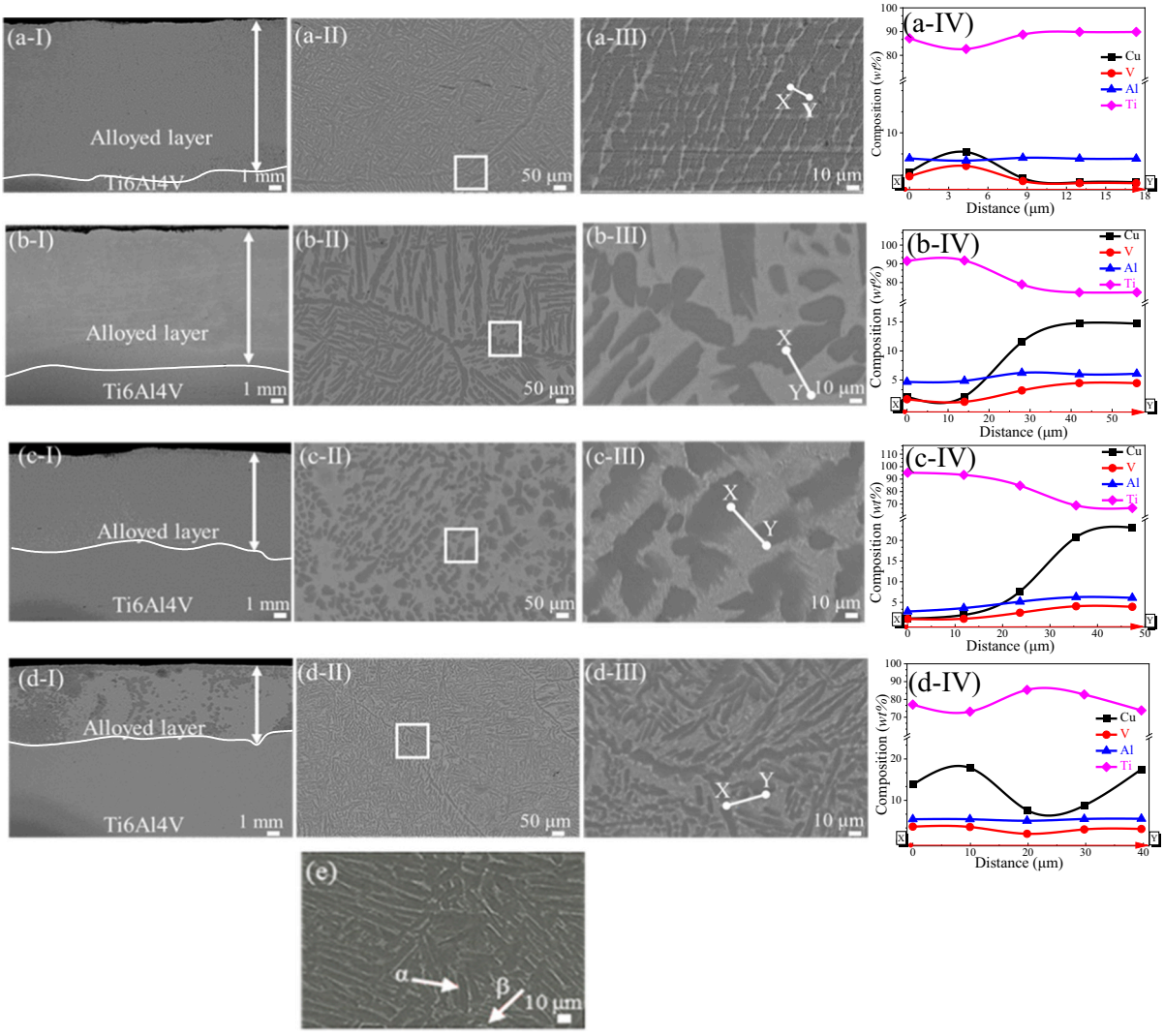

Fig. 6. Laser surface-alloyed specimens: (a) LA-Ti64-6Cu, (b) LA-Ti64-8Cu, (c) LA-Ti64-13Cu and (d) LA-Ti64-17Cu showing: (I) cross-sectional view, microstructure at (II) low magnification and (III) high magnification, and (IV) EDS scanning along XY and (e) microstructure of pristine Ti6Al4V.

contains about 90.55 at.% Ti, 5.43 at.% Al, 2.00 at.% V and 2.02 at.% Cu, is the α-Ti. The bright phases marked as D and E consist of 61.29 *at.*%/61.38 at.% Ti, 4.35 *at.*%/3.07 at.% Al, 2.81 *at.*%/1.33 *at.*% V and 31.55 at.%/34.22 at.% Cu, corresponding to $CuTi_2$. From Fig. 8(a-II), the other bright phase containing 50.21 at.% Ti, 1.97 at.% Al, 1.55 at.% V and 46.27 at.% Cu (marked as F) might be CuTi according to the Cu—Ti phase diagram [46].

3.2. Hardness

The microhardness profiles and average microhardness of the laser surface-alloyed specimens are shown in Fig. 9. The average values of microhardness of all laser surface-alloyed specimens are higher than that of the pristine Ti6Al4V (353 ± 6.5 $HV_{0.2}$) [47]. Among the laser surface-alloyed specimens, the average microhardness of LA-Ti64-17Cu is the highest, i.e. 646 ± 18 $HV_{0.2}$ and about 1.8 folds that of the pristine Ti6Al4V.

It is found that the average microhardness of the laser surface-alloyed specimens increases with the increase in Cu content, attributable to the existence of IMPs and grain refinement. Previous studies have shown that the $CuTi_2$ precipitates formed in sintered Ti—Cu alloys enhanced the microhardness and the mechanical strength [23]. Dong and his co-workers [13] reported that the hardness of the Ti—Cu alloys were approximately three times that of commercially pure Ti owing to the uniformly distributed $CuTi_2$ precipitates in the α-Ti matrix. In addition, it was proved that the presence of $CuTi_2$ in the Cu-bearing Ti6Al4V alloys led to its enhanced microhardness (397 ± 18 $HV_{0.1}$) as compared to that of the one without Cu (334 ± 9 $HV_{0.1}$) [48]. In the present study, strong convection was generated in the melt pool and led to uniform dispersion of the hard IMPs in the α-Ti matrix during LSA. IMPs (i.e. $CuTi_2$ and CuTi) are much harder than both the metallic phases (α-Ti and β-Ti). More IMPs means additional obstacles against the dislocation motion resulting in higher hardness [49,50]. Meanwhile, the hard IMPs in the Ti—Cu alloy could increase the dislocation pinning effect on grain boundary and then improve its hardness [39]. In addition, it was found that the grain size of α-Ti was significantly refined with Cu addition. Grain refinement was also an important factor to improve the strength of materials [51]. Therefore, the high contents of the IMPs ($CuTi_2$ and CuTi) in LA-Ti64-17Cu with the smallest grain size contributed to the highest microhardness. It is consistent with the finding of Zhang and his co-workers [52], reporting that a higher Cu content in the Ti—Cu alloy could provide a higher strength due to the existence of $CuTi_2$.

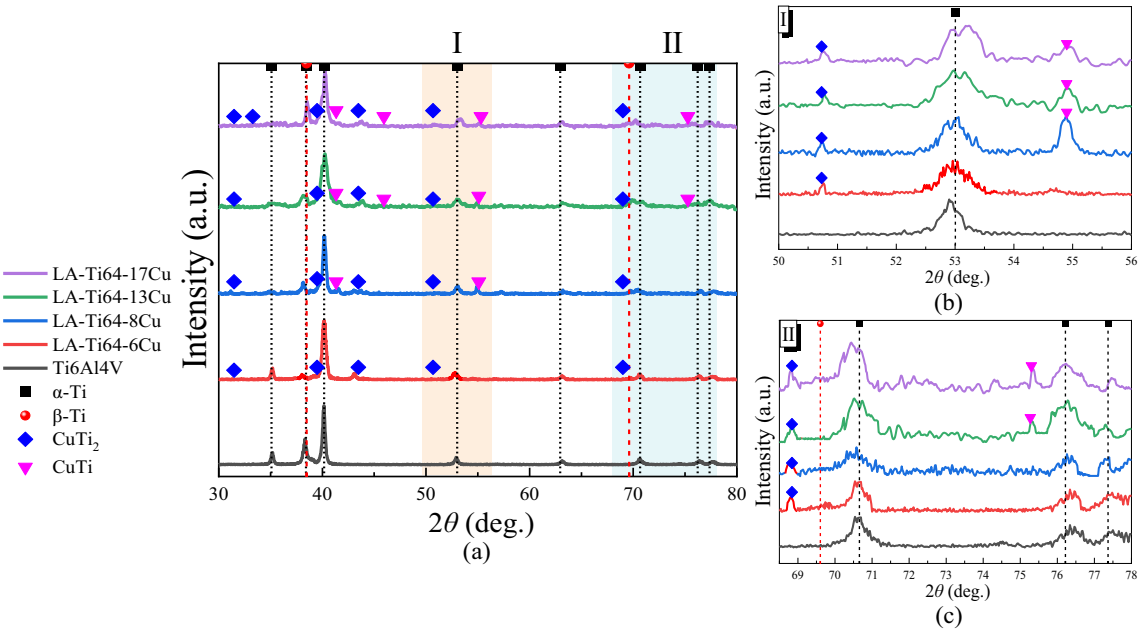

Fig. 7. (a) XRD patterns of pristine Ti6Al4V and various laser surface-alloyed Ti6Al4V with Cu. (b) and (c) show the magnified XRD patterns at the regions I and II marked in (a) respectively.

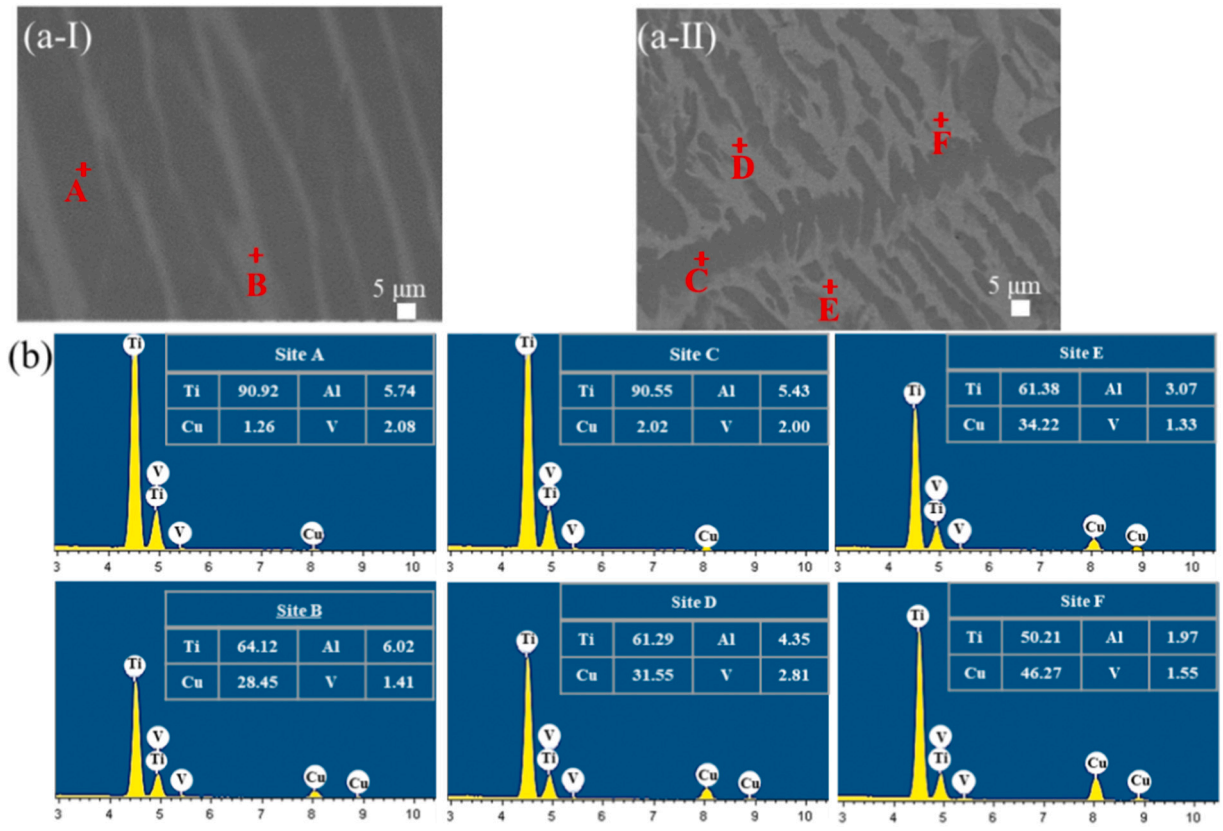

Fig. 8. SEM micrographs of (a-I) LA-Ti64-6Cu and (a-II) LA-Ti64-17Cu, (b) the EDS spectra and the content of elements at various sites (A to B for LA-Ti64-6Cu, C to F for LA-Ti64-17Cu).

3.3. Corrosion behavior

The corrosion behavior of the Ti6Al4V laser surface-alloyed with Cu in 0.9 wt% NaCl solution at 37 °C was investigated using electrochemical measurements. Fig. 10 shows the plot of open-circuit potential (E_{ocp}) vs time and the potentiodynamic polarization curves of the laser surface-alloyed specimens and pristine Ti6Al4V. The corrosion potential (E_{corr} vs. SCE) and corrosion current density (I_{corr}) extracted from the potentiodynamic polarization curves are listed in Table 3. E_{ocp} vs. SCE and E_{corr} vs. SCE of all specimens are very close. Also, it can be observed

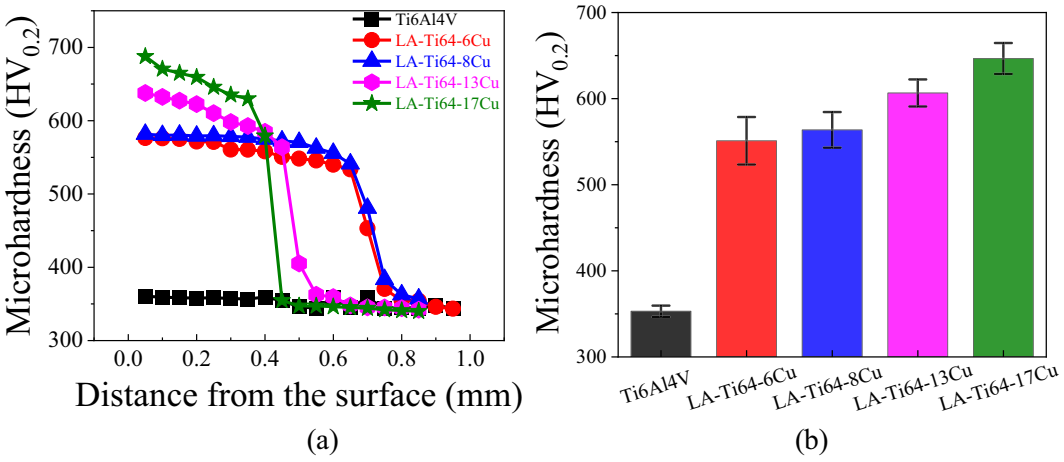

Fig. 9. (a) Microhardness profiles and (b) average microhardness of various laser surface-alloyed specimens.

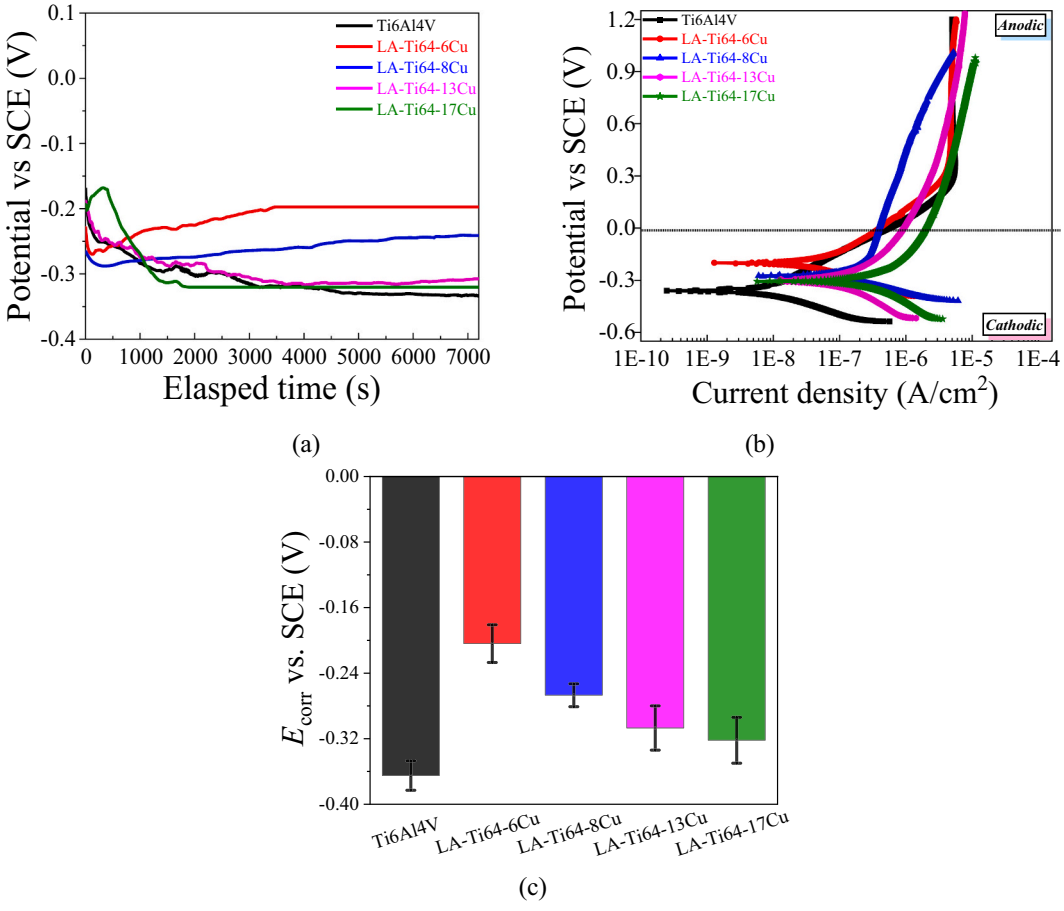

Fig. 10. (a) Plot of E_{OCP} vs. SCE against time, (b) potentiodynamic polarization curves and (c) E_{corr} vs. SCE of the laser surface-alloyed specimens in 0.9 *wt*% NaCl solution at 37 °C.

that the E_{ocp} vs. SCE and E_{corr} vs. SCE of the laser surface-alloyed specimens are nobler than that of the pristine Ti6Al4V due to the existence of the nobler IMPs [48,49]. As the Cu content increases, the E_{corr} vs. SCE increases at first to the noblest value (−0.204 V_{SCE}) for LA-Ti64-6Cu (Fig. 10(c)). After that the E_{corr} vs. SCE gradually shifts to a more active direction from −0.267 to −0.322 V_{SCE} as the Cu content increases from 8 to 17 wt%. On the other hand, the I_{corr} increases significantly as the Cu content increases. It is noticed that the I_{corr} of LA-Ti64-17Cu is the highest among all specimens. From Table 3, the I_{corr} of LA-Ti64-17Cu (2.01 μA/cm^2) is ~1932 times that of the pristine Ti6Al4V (0.00104 μA/cm^2). The corrosion rate (r) of LA-Ti64-17Cu (16.5×10^{-3} mm/yr) is ~1768 times that of the pristine Ti6Al4V (0.00933×10^{-3} mm/yr) based on Eqs. (3)–(5). According to the values of I_{corr} and the r, the ranking of corrosion resistance of the specimens is:

Pristine Ti6Al4V > LA-Ti64-6Cu > LA-Ti64-8Cu > LA-Ti64-13Cu > LA-Ti64-17Cu.

The Cu content of the laser surface-alloyed specimens directly affects the corrosion behavior. The IMP $CuTi_2$ was reported to be nobler than

Table 3
Corrosion parameters acquired from the polarization curves.

Specimen	E_{ocp} vs. SCE (V)	E_{corr} vs. SCE (V)	I_{corr} (μA/cm^2)	r (×10^{-3} mm/yr)
Ti6Al4V	−0.334 ± 0.035	−0.365 ± 0.018	0.00104 ± 0.0003	0.00933 ± 0.0026
LA-Ti64-6Cu	−0.197 ± 0.024	−0.204 ± 0.023	0.0618 ± 0.0041	0.5390 ± 0.0357
LA-Ti64-8Cu	−0.241 ± 0.019	−0.267 ± 0.014	0.521 ± 0.034	4.493 ± 0.293
LA-Ti64-13Cu	−0.307 ± 0.021	−0.307 ± 0.027	1.78 ± 0.10	14.9 ± 0.83
LA-Ti64-17Cu	−0.320 ± 0.020	−0.322 ± 0.028	2.01 ± 0.09	16.5 ± 0.73

α-Ti and this would lead to micro-galvanic corrosion in the α-Ti matrix for the SLMed Ti-xCu alloys (x = 0 to 10 wt%) [53]. Moreover, it was also confirmed that a higher Cu content in the vacuum-furnace melted Ti6Al4V-xCu alloys (x = 4.5–7.5 wt%) could lead to more $CuTi_2$, which were more cathodic than α-Ti and β-Ti. The formation of galvanic couples could lead to deterioration in corrosion resistance [54]. In the present study, it can be inferred that LA-Ti64-17Cu with the highest Cu content possesses the lowest corrosion resistance (highest I_{corr}) due to the micro-galvanic effect between the IMPs ($CuTi_2$ and CuTi) and α-Ti and β-Ti.

Fig. 11 illustrates the Nyquist, Bode impedance and phase angle plots of all laser surface-alloyed specimens and pristine Ti6Al4V. Their impedances are characterized by similar semi-circular capacitive loops reflecting that they are the typical passive alloys and consistent with the previous findings [22]. Fig. 11(a) shows that the diameter of the semi-circular arc of LA-Ti64-17Cu is the smallest, corresponding to the least resistive and the lowest polarization resistance. The EIS results are also displayed in the Bode plot (Fig. 11(b)) and Bode-phase representation (Fig. 11(c)). It can be seen that both the modulus of impedance (|Z|) and the phase angle show the same dependence for the laser surface-alloyed specimens with different Cu contents. It is known that the higher impedance and phase angle reflect a nobler electrochemical behavior for the specimens. Thus, it can be inferred that the corrosion resistance ranking is:

Pristine Ti6Al4V > LA-Ti64-6Cu > LA-Ti64-8Cu > LA-Ti64-13Cu > LA-Ti64-17Cu.

In order to provide quantitative support to the discussion on the EIS experimental results, an appropriate model (ZView software) for

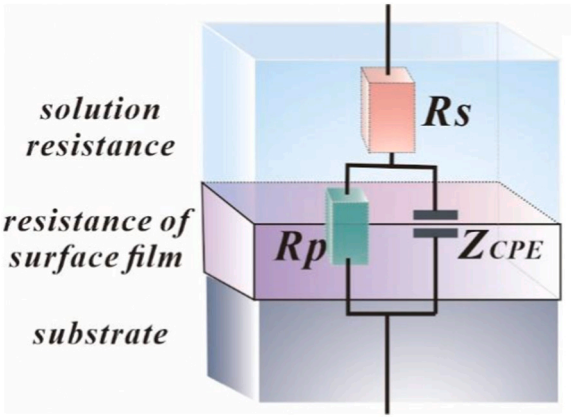

Fig. 12. The proposed equivalent circuit for modeling impedance parameters for the laser surface-alloyed specimens.

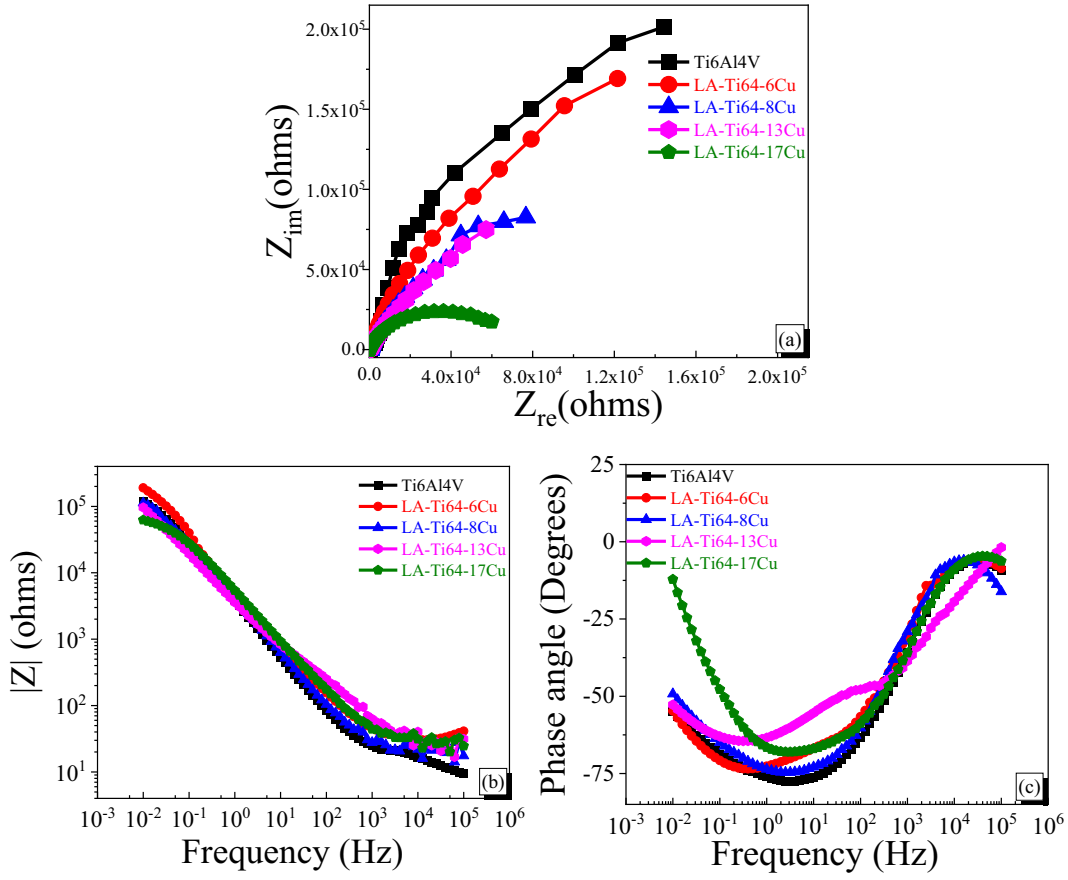

Fig. 11. (a) Nyquist plot, (b) Bode plot and (c) Bode-phase representation of the laser-alloyed specimens in 0.9 *wt*% NaCl solution at 37 °C.

equivalent circuit quantification has been used (Fig. 12). The phase angle between −70° and − 80° remained constant over a frequency range as shown in Fig. 11(c). Thus, the Randles' equivalent electrical circuit was applied to fit the EIS data under the passive condition [55]. Generally, $R_s(Q_pR_p)$ is used to describe the above model, where R_s is the electrolyte resistance, Q_p and R_p correspond to the capacitance and the polarization resistance of the passive film respectively. The induced passive film cannot be considered as an ideal capacitor and the constant-phase element (CPE) is widely used as a substitute for the ideal capacitor [56]. Hence, the relevant impedance (Z_{CPE}) and other parameters (R_s, n and R_p) obtained by the fitting procedure are applied to analyze the electrochemical performance of the laser-alloyed specimens. In addition, the value of Z_{CPE} is defined as follows [57]:

$$Z_{CPE} = \frac{1}{Y_0(j\omega)^n} \tag{9}$$

where j is the imaginary unit, ω is the angular frequency and Y_0 is the pseudo capacitance of the system. The parameter n is related to the phase angle due to the surface inhomogeneity and roughness of the materials, varying between −1 and 1 [58]. Based on the fitting of this model, the electrochemical parameters acquired from the EIS results are listed in Table 4. Meanwhile, the fitting quality is evaluated by the values of Chi-square (X^2) in the order of about 10^{-3}. The value of n obtained by fitting for the laser surface-alloyed specimens and pristine Ti6Al4V is in the range of 0.79 to 0.83, meaning that the films produced on the surfaces do not behave as a perfect capacitor [59]. Upon the testing condition of this work, there is a relationship between the radius of the semicircle and the charge transfer resistance or the polarization resistance (R_p) based on the results of the fitting model. Compared with the laser surface-alloyed specimens, the pristine Ti6Al4V with the largest radius of the semicircle shows the highest R_p ($6.13 \times 10^6\ \Omega\ cm^2$) as shown in Fig. 11(a), whereas LA-Ti64-17Cu with the smallest radius of the semicircle possesses the lowest R_p ($1.00 \times 10^6\ \Omega\ cm^2$). Combining the above analyses and the reported results [60], it can be proved that a higher R_p would provide a larger radius of the semicircle and higher corrosion resistance.

From Table 4, the value of the R_s is about 10^6 times smaller than R_p. Hence, the R_s could be neglected since such a small value would have little effect on the corrosion behavior of the specimens [61]. From the Bode plot [Fig. 11(b)], the |Z| plots of the laser-alloyed specimens are not smooth at high frequency. It is due to the formation of the oxide film on their surface. In the Bode phase angle plot (Fig. 11(c)), a trough could be observed in the middle frequency with the phase angle above −60°. This frequency range corresponds to the compactness of the produced oxide film. A compact oxide film is present on the surface when the phase angle is about −90°, and it can effectively inhibit charges transfer [62]. By comparing the flat portion of the laser surface-alloyed specimens, the flat portion of pristine Ti6Al4V is the widest and the corresponding phase angle is the largest (−75°). With the increase in Cu content, the trough region becomes narrower and the phase angle also shows a decreasing trend. Therefore, this phenomenon reveals that the stability of the oxide film formed on the specimens gradually decreases as the Cu content increases, and the stability of the oxide film of the LA-Ti64-17Cu is the lowest. To further evaluate the oxide films formed on the laser surface-alloyed specimens with various Cu contents, the thickness can be calculated by eq. (10) [63]:

$$d_{film} = \frac{\varepsilon\varepsilon_o A}{C_{eff}} \tag{10}$$

where ε is the dielectric constant of the oxide (TiO_2 is 60), ε_o is the permittivity of vacuum (8.85×10^{-14} F/m), A is the effective surface area and C_{eff} is the effective capacitance obtained from the fitted results (Z_{CPE}) using the software ZView. The calculated thickness of the oxide film produced on the laser surface-alloyed specimens with different Cu contents is shown in Table 4. The results indicate that the thickness becomes thinner as the Cu content increases. LA-Ti64-17Cu shows the thinnest oxide film which is also the most unstable and vulnerable to corrosion in the test solution. Based on the acquired value of R_p and relevant properties of the oxide film, the corrosion resistance ranking of the specimens in the 0.9 wt% NaCl solution at 37 °C is:

Pristine Ti6Al4V > LA-Ti64-6Cu > LA-Ti64-8Cu > LA-Ti64-13Cu > LA-Ti64-17Cu.

which is in good agreement with the polarization results.

Table 4
Parameters of equivalent circuits obtained by fitting the EIS experimental results.

	R_s (Ω cm^2)	Z_{CPE} (Ω^{-1} s^n cm^{-2})	n	R_p (Ω cm^2)	X^2	d_{film}(m)
Ti6Al4V	23.32	0.78×10^{-5}	0.8212	6.13×10^6	5.22×10^{-3}	68.08×10^{-8}
LA-Ti64-6Cu	25.48	1.12×10^{-5}	0.7948	5.67×10^6	1.44×10^{-3}	47.41×10^{-8}
LA-Ti64-8Cu	18.98	4.39×10^{-5}	0.8354	4.51×10^6	3.35×10^{-3}	12.10×10^{-8}
LA-Ti64-13Cu	26.27	5.41×10^{-5}	0.8116	1.92×10^6	1.44×10^{-3}	9.82×10^{-8}
LA-Ti64-17Cu	21.43	5.59×10^{-5}	0.8106	1.00×10^6	5.16×10^{-3}	9.50×10^{-8}

3.4. Corrosion morphology and mechanism

Fig. 13 shows the SEM micrographs of the laser surface-alloyed specimens after the polarization tests. More serious corrosion attack can be observed in the laser-alloyed specimens with a higher Cu content. The degree of corrosion attack in LA-Ti64-6Cu (Fig. 13(a)) and LA-Ti64-8Cu (Fig. 13(b)) is mild, and the attack initiates at the phase boundaries as displayed in the BSE images (Fig. 13(a-III)) and (Fig. 13(b-III)). Spalling of scales is observed in LA-Ti64-13Cu and the phase boundaries between the α/β-Ti and IMPs was attacked due to the stronger micro-galvanic effect (Fig. 13(c)). Spalling of scales and cracking can be observed in LA-Ti64-17Cu (Fig. 13(d-II)) as more active sites (i.e. α-Ti and β-Ti) led to more serious galvanic attack (Fig. 13(d-III)).

During polarization in the 0.9 wt% NaCl solution, the moving speed and exchange frequency of Cl^- ions in the test solution increased due to the effect of external voltage. Meanwhile, the metal ions (Al^{3+}, V^{5+}, Cu^+ and Ti^{4+}) would be leached from the laser surface-alloyed specimens at the beginning of anodic polarization. They would react with the Cl^- ions to produce the coordination compounds ($[AlCl_4]^-$, $[VCl_6]^-$, $[CuCl_2]^-$ and $[TiCl_6]^{2-}$) [64,65]. As their concentrations reach the critical levels, the corresponding metal oxides (Cu_2O, Al_2O_3, V_2O_5 and TiO_2) would form according to Eqs. (11)–(14). To a certain extent, the oxides formed on the surface of the laser surface-alloyed specimens behave as a passive film to inhibit corrosion in the NaCl solution. However, with different Cu contents, the effectiveness of the passive film varies.

$$2[AlCl_4]^- + 3H_2O \rightarrow Al_2O_3 + 6H^+ + 8Cl^- \tag{11}$$

$$2[VCl_6]^- + 5H_2O \rightarrow V_2O_5 + 10H^+ + 12Cl^- \tag{12}$$

$$2[CuCl_2]^- + H_2O \rightarrow Cu_2O + 2H^+ + 4Cl^- \tag{13}$$

$$[TiCl_6]^{2-} + 2H_2O \rightarrow TiO_2 + 4H^+ + 6Cl^- \tag{14}$$

From Fig. 10 to Fig. 13, the electrochemical corrosion behavior confirms that the increase in Cu content (6 to 17 wt%) in the laser surface-alloyed specimens leads to a higher corrosion rate as compared with pristine Ti6Al4V [23]. It can be inferred that the laser surface-alloyed specimens with higher Cu content contain more IMPs (cathodes) resulting in serious micro-galvanic attack of the phase boundaries between α/β-Ti and (anodes) and the IMPs (cathodes). The E_{corr} of LA-Ti64-6Cu shifted in the nobler direction due to the formation of more

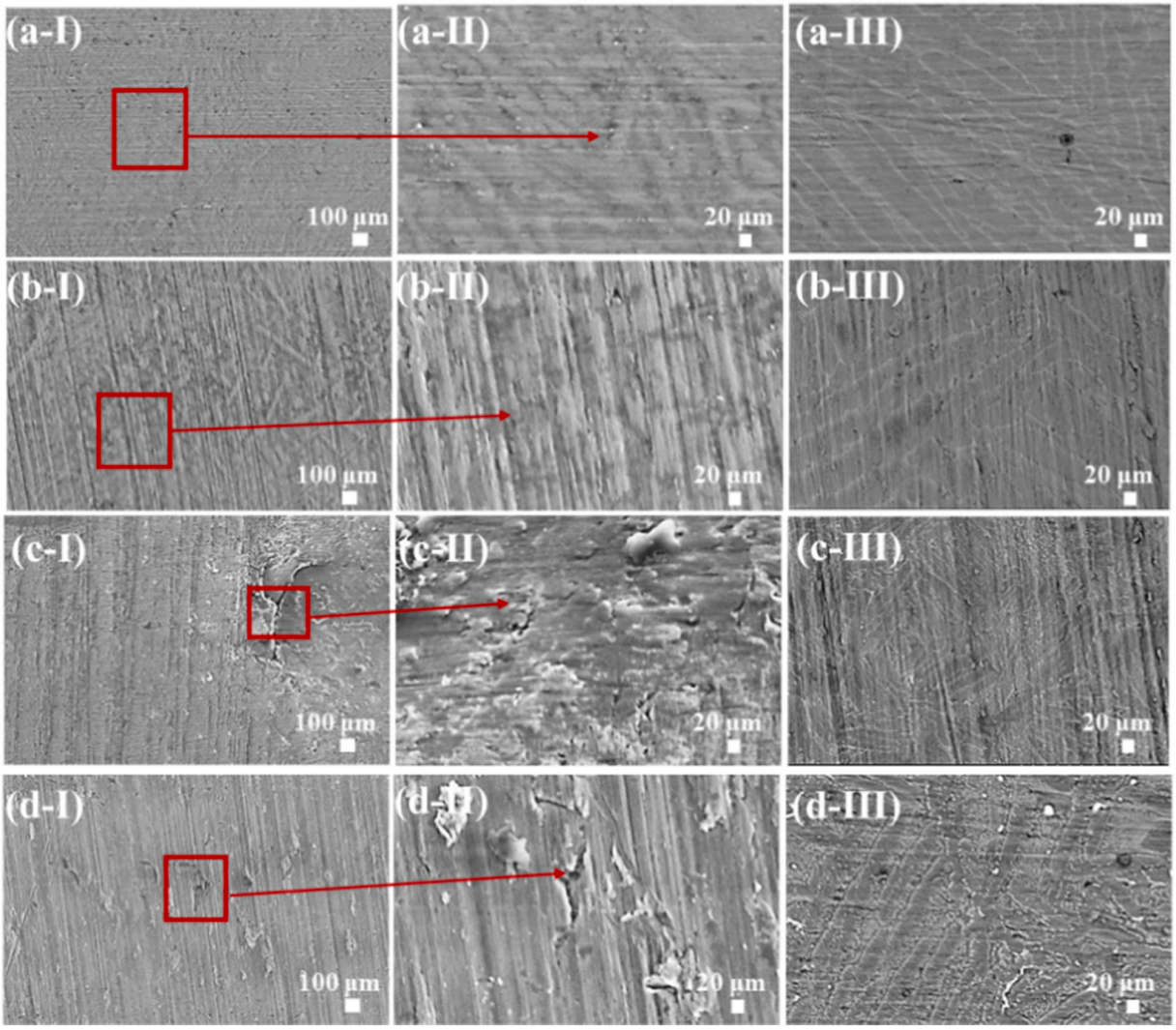

Fig. 13. Corrosion morphologies of (a) LA-Ti64-6Cu, (b) LA-Ti64-8Cu, (c) LA-Ti64-13Cu and (d) LA-Ti64-17Cu after polarization in 0.9 *wt*% NaCl solution at 37 °C under (I) low magnification, (II) high magnification and (III) the backscattered electron (BSE) images.

stable passive film (Cu_2O, Al_2O_3, V_2O_5 and TiO_2) on the surface. The oxides formed on the surface inhibited the dissolution of the LA-Ti64-6Cu leading to the lowest corrosion rate among the laser surface-alloyed specimens.

A schematic diagram depicted in Fig. 14 explains the corrosion mechanism. According to Fig. 14(a), the highest corrosion resistance of the pristine Ti6Al4V is due to the passive TiO_2 layer formed on the surface acting as a barrier against corrosion in NaCl solution as reported in the literature [66]. For the laser surface-alloyed specimens with a lower Cu content, e.g. LA-Ti64-6Cu, the micro-galvanic effect is less significant because the area of nobler IMPs is much smaller than that of the more active α/β-Ti (Fig. 14(b)). Then the protective film (Cu_2O, Al_2O_3, V_2O_5 and TiO_2) still plays the role in inhibiting corrosion, resulting in higher the corrosion resistance as evidenced by lower I_{corr}

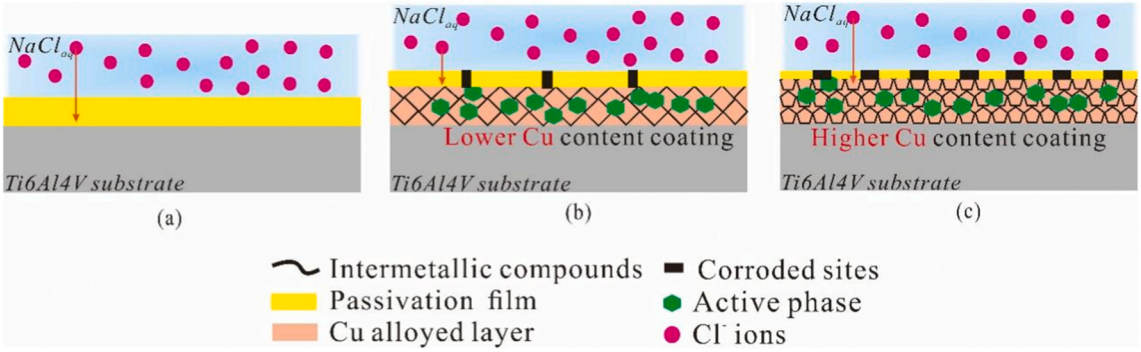

Fig. 14. Corrosion mechanisms for (a) pristine Ti6Al4V, (b) laser surface-alloyed specimens with a lower Cu content and (c) laser-alloyed specimens with a higher Cu content.

(Table 3) and higher R_p (Table 4). For the laser surface-alloyed specimens with a higher Cu content, e.g. LA-Ti64-17Cu [Fig. 14(c)], a larger area of the nobler IMPs ($CuTi_2$ and CuTi) than that of the more active α/β-Ti resulting in a more significant micro-galvanic effect. It leads to dissolution of a large amount of pre-formed passivation film (Cu_2O, Al_2O_3, V_2O_5 and TiO_2) [53]. Numerous cracking and spalling of scales are observed in LA-Ti64-17Cu (Fig. 13(d)) with the highest I_{corr}, lowest R_p, and thinnest d_{film} (Table 3 and Table 4).

4. Conclusions

In this study, laser surface alloying of Ti6Al4V with different Cu contents (6, 8, 13 and 17 wt%) has been successfully achieved using a HDPL. The results show that the Cu content in the laser surface-alloyed Ti6Al4V significantly affects the microstructure, hardness and corrosion behavior. With the increase in laser scanning speed and Cu content, finer grains and more IMPs ($CuTi_2$ and CuTi) are present in the laser surface-alloyed specimens leading to enhancement in hardness up to 646 ± 18 $HV_{0.2}$ (i.e. about 1.8 folds that of the pristine Ti6Al4V). According to values of the corrosion current density (I_{corr}), the corrosion resistance ranking of the laser surface-alloyed specimens in 0.9 wt% NaCl solution at 37 °C is: Ti6Al4V > LA-Ti64-6Cu > LA-Ti64-8Cu > LA-Ti64-13Cu > LA-Ti64-17Cu. LA-Ti64-6Cu possesses the highest corrosion resistance due to the lowest content of IMPs and less pronounced micro-galvanic effect, whereas the LA-Ti64-17Cu with the highest content of IMPs, has the lowest corrosion resistance due to the strongest micro-galvanic effect between the nobler IMPs and more active metallic phases (α-Ti and β-Ti). As Cu in the laser surface-alloyed Ti6Al4V possesses the anti-microbial efficacy, further study on their anti-bacterial and microbiologically influenced corrosion characteristics will attempted.

CRediT authorship contribution statement

Q. Qiao: Conceptualization, Validation, Investigation, Writing – original draft. **L.M. Tam:** Supervision, Investigation, Resources, Project administration, Writing – review & editing, Funding acquisition. **V.A.M. Cristino:** Supervision, Investigation, Writing – review & editing. **C.T. Kwok:** Conceptualization, Supervision, Investigation, Resources, Project administration, Writing – review & editing, Funding acquisition.

Declaration of competing interest

The authors declare that they have no known competing financial interests or personal relationships that could have appeared to influence the work reported in this paper.

Data availability

The data that has been used is confidential.

Acknowledgments

The present work was supported by the Science and Technology Development Fund (FDCT) of Macau SAR [File No. 0139/2020/A3] and the Institute for the Development and Quality, Macau.

References

[1] Y. Zhang, G.R. Ma, X.C. Zhang, Thermal oxidation of Ti-6Al-4V alloy and pure titanium under external bending strain: experiment and modelling, Corros. Sci. 122 (2017) 61–73.
[2] N.M. Lin, Q. Liu, J.J. Zou, D.L. Li, S. Yuan, Z.H. Wang, B. Tang, Surface damage mitigation of Ti6Al4V alloy via thermal oxidation for oil and gas exploitation application: characterization of the microstructure and evaluation of the surface performance, RSC Adv. 7 (22) (2017) 3517–3535.
[3] N.M. Lin, X.B. Huang, X.Y. Zhang, A.L. Fan, L. Qin, B. Tang, In vitro assessments on bacterial adhesion and corrosion performance of TiN coating on Ti6Al4V titanium alloy synthesized by multi-arc ion plating, Appl. Surf. Sci. 258 (18) (2012) 7047–7051.
[4] B.E. Carroll, T.A. Palme, A.M. Beese, Anisotropic tensile behavior of Ti-6Al-4V components fabricated with directed energy deposition additive manufacturing, Acta Mater. 87 (2015) 309–320.
[5] C.H.J. Hager, J.H. Sanders, S. Sharma, Unlubricated gross slip fretting wear of metallic plasma-sprayed coatings for Ti6Al4V surfaces, Wear 265 (2008) 439–451.
[6] C.D. Rabadia, Y.J. Liu, G.H. Cao, High-strength β stabilized Ti-Nb-Fe-Cr alloys with large plasticity, Mater. Sci. Eng. A 732 (2018) 368–377.
[7] J. Liu, L. Chang, H. Liu, Microstructure, mechanical behavior and biocompatibility of powder metallurgy Nb-Ti-Ta alloys as biomedical material, Mater. Sci. Eng. C 71 (2017) 512–519.
[8] M. Kikuchi, Y. Takada, S. Kiyosue, M. Yoda, M. Woldu, Z. Cai, T. Okabe, Mechanical properties and microstructures of cast Ti-Cu alloys, Dent. Mater. 19 (3) (2003) 174–181.
[9] Y.Z. Wan, G.Y. Xiong, H. Liang, S. Raman, F. He, Y. Huang, Modification of medical metals by ion implantation of copper, Appl. Surf. Sci. 253 (2007) 9426–9429.
[10] N. Huang, P. Yang, Y.X. Leng, J. Wang, H. Sun, J.Y. Chen, G.J. Wan, Surface modification of biomaterials by plasma immersion ion implantation, Surf. Coat. Technol. 186 (2004) 218–226.
[11] X.B. Zheng, Y.K. Chen, Y.T. Xie, H. Ji, L.P. Huang, C.X. Ding, Antibacterial property and biocompatibility of plasma sprayed hydroxyapatite/silver composite coating, J. Therm. Spray Technol. 18 (2009) 463.
[12] E.L. Zhang, F.B. Li, H.Y. Wang, J. Liu, C.M. Wang, M.Q. Li, K. Yang, A new antibacterial titanium copper sintered alloy: preparation and antibacterial property, Mater. Sci. Eng. C 33 (2013) 4280–4287.
[13] R. Dong, W.W. Zhu, C.C. Zhao, Y.W. Zhang, F.Z. Ren, Microstructure, mechanical properties, and sliding wear behavior of spark plasma sintered Ti-Cu alloys, Metall. Mater. Trans. A Phys. Metall. Mater. Sci. 49 (12) (2018) 6147–6160.
[14] L.E. Murr, S.A. Quinones, S.M. Gaytan, M.I. Lopez, A. Rodela, E.Y. Martinez, D. H. Hernandez, E. Martinez, F. Medina, R.B. Wicker, Microstructure and mechanical behavior of Ti6Al4V produced by rapid-layer manufacturing, for biomedical applications, J. Mech. Behav. Biomed. Mater. 20 (2009).
[15] Z. Yu, S. Yin, W. Zhang, X. Jiang, J. Hu, Picosecond laser texturing on titanium alloy for biomedical implants in cell proliferation and vascularization, J. Biomed. Mater. Res.B Appl. Biomater. 108 (2020) 1494–1504.
[16] D.I. Adebiyi, A.P.I. Popoola, Mitigation of abrasive wear damage of Ti-6Al-4V by laser surface alloying, Mater.Des. 74 (2015) 67–75.
[17] A.A. Siddiqui, A.K. Dubey, Recent trends in laser cladding and surface alloying, Opt. Laser Technol. 134 (2021), 106619.
[18] J.N. Li, C.Z. Chen, T. Squartini, Q.S. He, A study on wear resistance and microcrack of the Ti3Al/TiAl+TiC ceramic layer deposited by laser cladding on Ti6Al4V alloy, Appl. Surf. Sci. 257 (2010) 1550–1555.
[19] Y.J. Dong, H.M. Wang, Microstructure and dry sliding wear resistance of laser clad TiC reinforced Ti-Ni-Si intermetallic composite coating, Surf. Coat. Technol. 204 (2009) 731–735.
[20] S.M. Javadhesari, S. Alipour, M.R. Akbarpour, Biocompatibility, osseointegration, antibacterial and mechanical properties of nanocrystalline Ti-Cu alloy as a new orthopedic material, Colloids Surf. 189 (2020), 110889.
[21] L. Ren, Z. Ma, M. Li, Y. Zhang, W. Liu, Z. Liao, K. Yang, Antibacterial properties of Ti6Al4V-xCu alloys, J. Mater. Sci. Technol. 30 (7) (2014) 699–705.
[22] S. Guo, Y.J. Lu, S.Q. Wu, L.L. Liu, M.J. He, C.Q. Zhao, Y.L. Gan, J.J. Lin, X.C. Xu, J. X. Lin, Preliminary study on the corrosion resistance, antibacterial activity and cytotoxicity of selective-laser-melted Ti6Al4V-xCu alloys, Mater. Sci. Eng. C 72 (2017) 631–640.
[23] E. Zhang, X.Y. Wang, M. Chen, B. Hou, Effect of the existing form of Cu element on the mechanical properties, bio-corrosion and antibacterial properties of Ti-Cu alloys for biomedical application, Mater. Sci. Eng. C 69 (2016) 1210–1221.
[24] Y. Takada, O. Okuno, Corrosion characteristics of α-Ti and Ti2Cu composing Ti-Cu alloys, Dent. Mater. J. 24 (4) (2005) 610–616.
[25] W.R. Osório, A. Cremasco, P.N. Andrade, Electrochemical behavior of centrifuged cast and heat-treated Ti-Cu alloys for medical applications, Electrochim. Acta 55 (3) (2010) 759–770.
[26] C.T. Kwok, P.K. Wong, H.C. Man, Enhancement in corrosion and electrical wear resistance of copper via laser surface alloying with NiTi, Surf. Coat. Technol. 408 (2021), 126804.
[27] S. Singh, K.K. Pandey, V.K. Balla, Corrosion, wear and in-vitro biocompatibility property of surface mechanical attrition treatment processed Ti-6Al-4V alloy, JOM 73 (12) (2021) 4387–4396.
[28] ASTM G102-89 (2015) e1, Standard Practice for Calculation of Corrosion Rates and Related Information From Electrochemical Measurements, ASTM International, US, 2015.
[29] G.F. Sun, Y.K. Zhang, C.S. Liu, K.Y. Luo, X.Q. Tao, P. Li, Microstructure and wear resistance enhancement of cast steel rolls by laser surface alloying NiCr-Cr3C2, Mater.Des. 31 (6) (2010) 2737–2744.
[30] M.R. Bateni, S. Mirdamadi, F. Ashrafizadeh, J.A. Szpunar, R.A.L. Drew, Formation of novel Ti-Cu intermetallic coatings on copper substrate, Mater. Manuf. Process. 16 (2001) 219–228.
[31] G.K. Dey, A. Biswas, S.K. Roy, S. Banerjee, Rapid solidification effects during micropyretic synthesis of Ti50Cu50 intermetallic compound, Mater. Sci. Eng. A 304–306 (2001) 641–645.
[32] O.S. Fatoba, S.A. Akinlabi, E.T. Akinlabi, M.F. Erinosho, Influence of process parameters on the mechanical properties of laser deposited Ti-6Al-4V alloy. Taguchi and response surface model approach, Mater. Today 5 (2018) 19181–19190.

[33] S.A. Akinlabi, M.P. Mashinini, O.S. Fatoba, E.T. Akinlabi, Characterization of corrosion behaviour of laser beam formed titanium alloy, IOP Conf.Ser.Mater.Sci. Eng. 423 (2018), 012174.
[34] E.W. Collings, H.L. Gegel, Physical principles of solid solution strengthening in alloys, in: Physics of Solid Solution Strengthening, Springer, Boston, MA, 1975, pp. 147–182.
[35] H.P. Ng, P. Nandwana, A. Devaraj, Conjugated precipitation of twin-related α and Ti2Cu phases in a Ti-25V-3Cu alloy, Acta Mater. 84 (2015) 457–471.
[36] H. Donthula, B. Vishwanadh, T. Alam, Morphological evolution of transformation products and eutectoid transformation (s) in a hyper-eutectoid Ti-12 at% Cu alloy, Acta Mater. 168 (2019) 63–75.
[37] V.S. Aigbodion, A.P.I. Popoola, O.S. Fatoba, Evaluation of hardness values and corrosion behavior of laser alloyed 20Al-20Sn-60Ti coatings of UNS G10150 mild steel, Int. J. Adv. Manuf. Technol. 86 (2016) 291–301.
[38] W. Zong, S. Zhang, C. Zhang, Design and characterization of selective laser-melted Ti6Al4V-5Cu alloy for dental implants, Mater. Corros. 71 (10) (2020) 1697–1710.
[39] Y. Xu, J. Jiang, Z. Yang, The effect of copper content on the mechanical and tribological properties of hypo-, hyper-and eutectoid Ti-Cu alloys, Materials 13 (15) (2020) 3411.
[40] M.R. Akbarpour, H.M. Mirabad, A. Hemmati, H.S. Kim, Processing and microstructure of Ti-Cu binary alloys: a comprehensive review, Prog. Mater. Sci. 100933 (2022).
[41] X. Wang, L.J. Zhang, J. Ning, Effect of Cu-induced eutectoid transformation on microstructure and mechanical properties of Ti-6Al-4V alloy by laser wire deposition, Mater. Sci. Eng. C 142316 (2021).
[42] X. Gong, J. Lydon, K. Cooper, K. Chou, Beam speed effects on Ti-6Al-4V microstructures in electron beam additive manufacturing, J. Mater. Res. 29 (2014) 1951–1959.
[43] M.E. Makhatha, O.S. Fatoba, E.T. Akinlabi, Effects of rapid solidification on the microstructure and surface analyses of laser deposited Al-Sn coatings on AISI 1015 steel, Int. J. Adv. Manuf. Technol. 94 (2018) 773–787.
[44] O.S. Fatoba, A.P.I. Popoola, V.S. Aigbodion, Experimental study of hardness values and corrosion behavior of laser alloyed Zn-Sn-Ti coatings of UNS G10150 mild steel, J. Alloys Compd. 658 (2016) 248–254.
[45] P.A. Kobryn, S.L. Semiatin, Microstructure and texture evolution during solidification processing of Ti-6Al-4V, J. Mater. Process. Technol. 135 (2–3) (2003) 330–339.
[46] M.R. Bateni, F. Ashrafizadeh, J.A. Szpunar, R.A.L. Drew, Improving the tribological behavior of copper through novel Ti-Cu intermetallic coatings, Wear 253 (5–6) (2002) 626–639.
[47] G. Ma, C. Yu, Y. Li, F. Niu, D. Wu, G. Bi, S. Liu, High-mass-proportion TiCp/Ti6Al4V titanium matrix composites prepared by directed energy deposition, Addit. Manuf. 35 (2020), 101323.
[48] S. Wang, Z. Ma, Z.H. Liao, J. Song, K. Yang, W.Q. Liu, Study on improved tribological properties by alloying copper to Cp-Ti and Ti-6Al-4V alloy, Mater. Sci. Eng. C 57 (2015) 123–132.
[49] F. Weng, H.J. Yu, C.Z. Chen, J.L. Liu, L.J. Zhao, J.J. Dai, Effect of process parameters on the microstructure evolution and wear property of the laser cladding coatings on Ti-6Al-4V alloy, J. Alloys Compd. 692 (2017) 989–996.
[50] S.G. Tabrizi, S.A. Sajjadi, A. Babakhani, W.J. Lu, Analytical and experimental investigation of the effect of SPS and hot rolling on the microstructure and flexural behavior of Ti6Al4V matrix reinforced with in-situ TiB and TiC, J. Alloys Compd. 692 (2017) 734–744.
[51] Y.M. Ren, X. Lin, X. Fu, Microstructure and deformation behavior of Ti-6Al-4V alloy by high-power laser solid forming, Acta Mater. 132 (2017) 82–95.
[52] W. Zhang, S. Zhang, H. Liu, Effects of surface roughening on antibacterial and osteogenic properties of Ti-Cu alloys with different cu contents, J. Mater. Sci. Technol. 88 (2021) 158–167.
[53] H. Ji, M.C. Zhao, B. Xie, Corrosion and antibacterial performance of novel selective-laser-melted (SLMed) Ti-xCu biomedical alloys, J. Alloys Compd. 864 (2021), 158415.
[54] C. Peng, Y. Liu, H. Liu, Optimization of annealing treatment and comprehensive properties of Cu-containing Ti6Al4V-xCu alloys, J. Mater. Sci. Technol. 35 (10) (2019) 2121–2131.
[55] F. Rosalbino, G. Scavino, Corrosion behavior assessment of cast and HIPed Stellite 6 alloy in a chloride-containing environment, Electrochim. Acta 111 (2013) 656–662.
[56] H. Bouchemel, A. Benchettara, Corrosion behavior of a new Ti–3Mo alloy in simulated body fluid for biomedical applications, Arab. J. Sci. Eng. 39 (1) (2014) 139–146.
[57] A. Kocijan, D.K. Merl, M. Jenko, The corrosion behaviour of austenitic and duplex stainless steels in artificial saliva with the addition of fluoride, Corros. Sci. 53 (2) (2011) 776–783.
[58] H.C. Hsu, S.C. Wu, S.K. Hsu, Effects of heat treatments on the structure and mechanical properties of Zr-30Ti alloys, Mater. Charact. 62 (2) (2011) 157–163.
[59] A.M. Fekry, The influence of chloride and sulphate ions on the corrosion behavior of Ti and Ti-6Al-4V alloy in oxalic acid, Electrochim. Acta 54 (12) (2009) 3480–3489.
[60] Y. Lu, L. Ren, X. Xu, Effect of Cu on microstructure, mechanical properties, corrosion resistance and cytotoxicity of CoCrW alloy fabricated by selective laser melting, J. Mech. Bechav. Biomed. (2018) 130–141.
[61] S. Karimi, T. Nickchi, A. Alfantazi, Effects of bovine serum albumin on the corrosion behaviour of AISI 316L, Co-28Cr-6Mo, and Ti-6Al-4V alloys in phosphate buffered saline solutions, Corros. Sci. 53 (10) (2011) 3262–3272.
[62] A.C. Alves, F. Wenger, P. Ponthiaux, J.P. Celis, A.M. Pinto, L.A. Rocha, J.C. S. Fernandes, Corrosion mechanisms in titanium oxide-based films produced by anodic treatment, Electrochim. Acta 234 (2017) 16–27.
[63] Y. Lu, S. Guo, Y. Yang, Y.J. Liu, Y. Zhou, S.Q. Wu, C.Q. Zhao, J.X. Lin, Effect of thermal treatment and fluoride ions on the electrochemical corrosion behavior of selective laser melted CoCrW alloy, J. Alloys Compd. 730 (2018) 552–562.
[64] E.M. Sherif, S.M. Park, Inhibition of copper corrosion in 3.0% NaCl solution by N-phenyl-1, 4-phenylenediamine, J. Electrochem. Soc. 152 (10) (2005) B428.
[65] Y. Hu, H. Chen, X. Liang, Titanium fabricated by selective laser melting: microstructure, wear and corrosion behavior in different orientations, Rapid Prototyp.J. 28 (3) (2022) 546–558.
[66] R.M.A. Shahba, W.A. Ghannem, A.E.S. El-Shenawy, A.S.I. Ahmed, S.M. Tantawy, Corrosion and inhibition of Ti-6Al-4V alloy in NaCl solution, Int. J. Electrochem. Sci. 6 (2011) 5499–5509.